PASJ: Publ. Astron. Soc. Japan **60**, S375–S388, 2008 December 25

Absolute Photometric Calibration of the Infrared Camera (IRC) aboard AKARI

Toshihiko TANABÉ,[1] Itsuki SAKON,[2] Martin COHEN,[3] Takehiko WADA,[4] Yoshifusa ITA,[5]
Youichi OHYAMA,[4*] Shinki OYABU,[4] Kazunori UEMIZU,[4] Toshinobu TAKAGI,[4] Daisuke ISHIHARA,[2]
Woojung KIM,[4†] Munetaka UENO,[6] Hideo MATSUHARA,[4] and Takashi ONAKA[2]
[1]*Institute of Astronomy, Graduate School of Science, The University of Tokyo, 2-21-1 Osawa, Mitaka, Tokyo 181-0015*
ttanabe@ioa.s.u-tokyo.ac.jp
[2]*Department of Astronomy, Graduate School of Science, The University of Tokyo, 7-3-1 Hongo, Bunkyo-ku, Tokyo 113-0033*
[3]*Radio Astronomy Laboratory, 601 Campbell Hall, University of California, Berkeley, CA 94720, USA*
[4]*Institute of Space and Astronautical Science, Japan Aerospace Exploration Agency,*
3-1-1 Yoshinodai, Sagamihara, Kanagawa 229-8510
[5]*National Astronomical Observatory of Japan, National Institutes of Natural Sciences,*
2-21-1 Osawa, Mitaka, Tokyo 181-8588
[6]*Department of Earth Science and Astronomy, Graduate School of Arts and Sciences, The University of Tokyo,*
3-8-1 Komaba, Meguro, Tokyo 153-8902

(Received 2008 August 1; accepted 2008 October 6)

Abstract

The absolute photometric calibration of imaging observations with the Infrared Camera (IRC) aboard the AKARI satellite was performed by monitoring the same stars regularly and by observing a set of standard stars. By our monitoring observations, we confirmed that all channels of the IRC were stable to within 4% and that their sensitivities were constant until the liquid helium was exhausted. Using the data of these repeated observations, we evaluated the intrinsic errors as a function of the brightnesses of objects and found that the errors increase rapidly toward fainter objects. We also checked the consistency between short and long exposure times, and confirmed that the data sampling had been executed as designed. Finally, by comparing the estimated in-band flux densities and the observed data values of standard stars, we obtained conversion factors to the absolute flux densities of all the band/exposure configurations. Their absolute uncertainties are estimated to be less than 6%.

Key words: infrared: general — space vehicles: instruments — techniques: photometric

1. Introduction

The Japanese infrared satellite AKARI (Murakami et al. 2007) was launched on 2006 February 21 (UT). The aperture lid was opened on 2006 April 13, after which AKARI began to observe the sky. After a performance verification, Phase 1, which was dedicated to the All-Sky Survey in the far-infrared, began on 2006 May 8. Six months later, Phase 2 started on 2006 November 9 for both All-Sky Survey and Mission Programs. AKARI's liquid-helium supply ran out and Phase 2 ended on 2007 August 26. After Phase 2, only near-infrared observations will be executed under somewhat different conditions, and their calibration should be done separately.

The Infrared Camera (IRC) (Onaka et al. 2007) is one of two focal-plane instruments aboard the AKARI satellite. It was designed for wide-field imaging and low-resolution spectroscopy at near- to mid-infrared wavelengths (1.8–26.5 μm) in the pointed observation mode of AKARI. The IRC was also operated in the survey mode to make an All-Sky Survey at 9 μm and 18 μm during Phase 1 and Phase 2. We here describe the in-flight absolute flux calibration of the IRC in the imaging mode. This paper is confined to the imaging observations in the pointing mode. The calibration of the All-Sky Survey mode will be presented in a paper by D. Ishihara et al. (in preparation). The performance and the in-flight calibration of the spectroscopy is described in Ohyama et al. (2007).

The IRC consists of three channels (NIR, MIR-S, and MIR-L) each of which has three broad-band filters, enabling us to make imaging observations with three different filters sequentially. Their calibrations were performed with two kinds of observations: monitoring nonvariable stars and imaging absolutely calibrated standard stars. The former was intended to check the stability of the sensitivity by observing identical stars in the same fields regularly in all bands. The latter was to find the conversion factors from the observed data values (instrumental value in an analog-to-digital unit; hereafter ADU) to the absolute flux densities of all the band/exposure configurations by comparing the observed and estimated brightnesses of a set of standard stars.

In section 2, first we briefly describe the methods of signal reading and IRC data products. In section 3, we describe our observations and data reduction. We also list standard stars. In section 4, we present the result of a stability check, and give the conversion factors. Here, we checked the consistency between short and long exposure times to confirm that both data sets are usable simultaneously for the absolute calibration. We also discuss the intrinsic errors of the IRC camera and the AKARI magnitude system.

* Present address: Academia Sinica, Institute of Astronomy and Astrophysics, PO Box 23-141, Taipei 106, Taiwan, R.O.C.
† Present address: Semiconductor business group, Sony corporation, Atsugi, Kanagawa 243-0014.

2. IRC Pointing Observations and Data Products

The focal-plane array operation is described in ASTRO-F Observer's Manual,[1] and in Onaka et al. (2007) in detail. Here, we briefly explain it for a better understanding of IRC data products. In the pointing mode, a combination of the exposure, filter exchange and dithering operations is fixed to several patterns, which are called Astronomical Observation Template (AOT). The IRC AOT is designated as IRCxx, where xx indicates the AOT number. For imaging observations, three AOTs are used: a three-filter mode IRC03, a two-filter mode IRC02 and a one-filter mode IRC05 (originally IRC00). In any AOT, a unit of the exposure pattern is repeated several times. This unit is called "exposure frame" (in Onaka et al. 2007) (or "exposure cycle" in Observer's Manual). The unit exposure frame, except for IRC05, is called the standard frame while that for IRC05 is called the IRC05 frame. One standard frame of the NIR channel consists of one short exposure and one long exposure. That of MIR-S and MIR-L consists of one short exposure and three long exposures; the durations of both exposures are different from those of the NIR channel. One IRC05 frame of the NIR channel consists of one short exposure (same as the standard frame) and one long exposure which is different from that of the standard frame. That of the MIR-S and MIR-L channels consists of two standard frames of the MIR-S and MIR-L, i.e., two short exposures and six long exposures (see figure 6 of Onaka et al. 2007). The operation of the MIR-S and MIR-L arrays is controlled by the same clock, and we can treat both exposures as being the same one, although the arrays are different. Therefore, there are five kinds of exposures in total: one short exposure and two long exposures in the NIR channel and one short exposure and one long exposure in the MIR channels.

Here, we describe the methods for reading signals and the exposure times. In any one exposure, data are taken using a Fowler sampling method (Fowler & Gatley 1990) to reduce the read noise. The Fowler N sampling method consists of N non-destructive reads after a reset (pedestal reads) and another N non-destructive reads near the end of the integration (signal reads). The sum of signal reads is subtracted from the sum of pedestal reads and transmitted to the ground. The Fowler 4 sampling is employed for a long exposure in the standard frame while the Fowler 16 sampling is carried out for a long exposure in the IRC05 frame. For short exposures, data are taken with the Fowler 1 sampling. The pedestal reads of the short exposure are slightly different from those of the long one. Since the pedestal reads for a short exposure are taken immediately after the reset, it could be affected by the reset operation. Therefore, the consistency between short and long exposure times needs to be checked. The time interval between signal reads and pedestal reads corresponds to the duration of an exposure. Because any array is driven in the unit of one fixed time interval, the durations of any exposure are an integral multiple of this unit time length. We call this time length the IRC time unit, $t_{\rm IRC}$, and this integer as a unit number. Thus, the individual exposure time, $t_{\rm exp}$, can be expressed as $t_{\rm IRC}$ times the unit number. The IRC time unit was measured to be about 0.5844 s in the pre-flight experiment. The unit number and $t_{\rm exp}$ of each channel/exposure configuration is tabulated in table 1. Basically, we calibrated these five exposure data separately. We discuss the consistency between short and long exposure in subsection 4.3. We then show in subsection 4.4 the absolute calibration using both short and long exposure data simultaneously. For this purpose, we introduce ADU values per IRC time unit, $N^{*}_{\rm ADU} \equiv N_{\rm ADU} t^{-1}_{\rm IRC}$, which is defined as $N_{\rm ADU}$/(the unit number), where $N_{\rm ADU}$ is the total number of ADUs resulting from the photometry. We call it a *normalized* ADU value.

Table 1. Unit number and exposure time of each channel / exposure configuration.

Channel	Exposure	Unit number	$t_{\rm exp}$
NIR	short	8	4.6752
	long	76	44.4144
	long (IRC05)	112	65.4528
MIR	short	1	0.5844
	long	28	16.3632

We describe in more detail the actual data contents. In the NIR channel, the data values in the RAW frames of long exposures taken with IRC02 and IRC03 are 4-folded because of the Fowler 4 sampling, as mentioned above. We drop the least-significant 2 bits to reduce the data rate (2-bit-shift) in the Fowler 16 mode, and thus the long exposure of IRC05 is 4-fold instead of 16-fold. The same bit shift is applied for the IRC05 short frame as well, and thus the data values have been reduced by 4. In the case of MIR channels, the data in the raw frames of all short exposures have been reduced by 4 owing to the 2-bit-shift. However, the IRC pipeline produces one co-added image for each band / exposure configuration by taking their median (or average) of $N_{\rm coadd}$ images and the exposure time of the final data product corresponds to $t_{\rm exp}$ tabulated in table 1. Note that the actual integrated exposure time is, of course, $t_{\rm exp}$ times the number of co-added frames, $N_{\rm coadd}$.

3. Observations and Data Reduction

For checking the stability of the IRC, we chose one North Ecliptic Pole (NEP) region (center: $\alpha \sim 17^{\rm h}55^{\rm m}24^{\rm s}$, $\delta \sim 55°37'32''$), for NIR and MIR-S bands and one South Ecliptic Pole (SEP) region (center: $\alpha \sim 6^{\rm h}00^{\rm m}49^{\rm s}$, $\delta \sim -66°36'14''$) for MIR-L bands. Because the orbit of the AKARI is Sun-synchronous, only the regions towards the ecliptic poles can be observed at any time. However, each field contains at least several stars suitable for monitoring the brightnesses in each band. We found several stars to be suspected variables and did not use them for the stability check. The NEP field had been monitored since 2006 June 19 to 2007 August 1, in total 31 times, while the SEP field was observed from 2006 August 7 to 2007 July 16, in total 24 times. Both observations had been made on a once-a-week basis until late August in 2006, and later switched to twice a month. These observations were carried out with IRC03 (three-filter mode), which performed either imaging in all of the NIR and MIR-S bands or all of

[1] Available at ⟨http://www.ir.isas.jaxa.jp/ASTRO-F/Observation/ObsMan/afobsman32.pdf⟩.

Table 2. Observed NEP and SEP standard stars.

Star*	2MASS ID	Spectrum	K_s	Observation date (UT)	Observation ID
for NIR, MIR-S					
HD 42525	06060937−6602227	A0 V	5.751	2006-04-22 04:08:28	5020008.1
NPM1 +60.0581	17245227+6025508	A1 V	9.645	2007-02-13 23:48:41	5124042.1
1757132	17571324+6703409	A3 V	11.155	2006-04-26 22:49:47	5020001.1
KF 03T1	17574394+6626553	K0 III	9.923	2006-08-03 19:30:00	5124019.1
KF 03T2	17575147+6631034	K1.5 III	8.963	2006-08-03 19:30:00	5124019.1
KF 06T1	17575849+6652293	K1.5 III	10.872	2006-04-26 19:31:48	5020002.1
KF 06T2	17583798+6646522	K1.5 III	11.149	2006-04-26 19:31:48	5020002.1
KF 06T3	17585021+6649406	K1 III	10.348	2006-04-26 19:31:48	5020002.1
KF 06T3 2				2006-07-06 19:15:10	5124009.1
KF 03T3	17590114+6633262	K1.5 III	10.925	2006-08-11 19:08:13	5124020.1
KF 03T4	17590395+6630593	K1 III	10.091	2006-08-11 19:08:13	5124020.1
KF 09T1	17592304+6602561	K0 III	8.114	2007-04-15 02:03:34	5124054.1
KF 09T1 2				2007-06-02 01:28:46	5124106.1
KF 06T4	17592606+6654581	K0 III	11.240	2006-07-06 19:15:10	5124009.1
KF 01T4	18040314+6654459	K1.5 III	8.067	2006-06-24 19:55:00	5124007.1
KF 01T4 2				2007-04-15 00:24:01	5124052.1
KF 01T4 3				2007-06-01 00:37:25	5124107.1
KF 01T5	18040388+6655437	K1 III	11.072	2006-06-24 19:55:00	5124007.1
KF 01T5 2				2007-04-15 00:24:01	5124052.1
KF 01T5 3				2007-06-01 00:37:25	5124107.1
for MIR-L					
HD 42525	06060937−6602227	A0 V	5.751	2006-04-22 02:03:59	5020009.1
NPM1 +65.0451	16533704+6538175	K2 III	6.524	2006-12-20 01:36:45	5124037.1
HD 158485	17260484+5839069	A3 V	6.145	2006-08-22 17:47:59	5124022.1
BD +66 1060	17560018+6655430	K2 III	6.720	2006-11-07 16:16:54	5124031.1
NPM1 +67.0536	17585466+6747368	K2 III	6.409	2006-04-24 14:43:03	5020005.1
HD 165459	18023073+5837381	A1 V	6.584	2007-03-22 01:44:58	5124043.1
BD +66 1073	18030959+6628119	K1 III	7.544	2006-06-28 19:41:30	5124006.1
KF 01T4	18040314+6654459	K1.5 III	8.067	2006-06-24 23:13:10	5124008.1
HD 166780	18083882+5758468	K4 III	3.963	2006-09-29 19:43:33	5124021.1

* The designations of star names are the following: KF denotes the Kummel field number from the north ecliptic pole optical/near-infrared survey by Kümmel and Wagner (2000) in which Kümmel and Cohen sought K-giants, NPM 1 from the Lick Northern Proper Motion program by Klemola, Jones, and Hanson (1987), 1757132 from 2MASS.

the MIR-L bands. Besides these monitoring observations, the same NEP field was observed 10 times in the *N3* and *S7* bands within one week in the Performance Verification Phase. These data were used for checking the short-term stability. These observations were made with IRC00 (one-filter mode, later replaced by IRC05).

For the absolute flux calibration, we observed a set of standard stars in the ecliptic pole regions which were established for Spitzer IRAC by Cohen and his collaborators (Cohen et al. 1996, 1999, 2003a, 2003b; Cohen 2003). We list the observed NEP and SEP standards in table 2 along with the 2MASS ID, spectral type, 2MASS K_s magnitude, observed date, and AKARI observation ID. These observations were also carried out with IRC03. In addition to these data, we have included standard stars in the Large Magellanic Cloud. About an area of 10 deg^2 in the LMC had been surveyed by one of the AKARI's Large-Area Survey projects, the ASTRO-F Large Area Survey of the Magellanic Cloud (LSLMC: Ita et al. 2008). The standard stars in the LMC, the so-called SAGE standards, were also established by Cohen in IRAC and MIPS24 for the Spitzer SAGE program (Meixner et al. 2006; Cohen et al. 2003b). The latter data were taken with IRC02 (two-filter mode) and only *N3*, *S7*, *S11*, *L15*, and *L24* data are available. The SAGE standards used are tabulated in table 3.

For checking the consistency between short and long exposures in the NIR channel in the case of IRC05, we also used the data obtained for another Large-Area Survey project, the ASTRO-F NEP Survey (LSNEP: Matsuhara et al. 2007).

Raw data were processed with the IRC imaging data pipeline, version 070104 (IRC Data User's Manual).[2] The pipeline produces one co-added image for each band/exposure configuration, using "median" as the combine mode. For photometry, we applied aperture photometry independently to the co-added image using the IRAF[3] package PHOT task. The radius of the aperture adopted is 10 pixels for NIR bands and

[2] ⟨http://www.ir.isas.jaxa.jp/ASTRO-F/Observation/#IDUM⟩.

[3] IRAF is distributed by the US National Optical Astronomy Observatories, which are operated by the Association of Universities for Research in Astronomy, Inc., under cooperative agreement with the National Science Foundation.

Table 3. SAGE standard stars.

Star	2MASS ID	Spectrum	K_s	Observation date (UT)	Observation ID
for *N3*, *S7*, *S11*					
HD 34461	05121801−6705415	K1 III	6.927	2006-06-08 18:21:09	2200079.1
HD 34555	05125331−6744362	A3 V	9.288	2006-05-31 05:38:19	2200060.1
HD 34943	05153759−6804070	M0 III	3.970	2006-05-26 06:46:47	2200049.1
HD 269247	05154596−6750148	K0 III	8.817	2006-05-28 06:39:13	2200054.1
HD 35094	05164382−6811142	A3 V	8.554	2006-05-23 07:47:52	2200042.1
HD 35094 2				2006-05-25 06:01:07	2200046.1
HD 35183	05172303−6828190	A3 V	8.754	2006-05-20 23:40:20	2200037.1
HD 35323	05183268−6732320	M0 III	5.524	2006-11-29 13:25:55	2200049.1
HD 269352	05193283−6752441	K5 III	6.014	2006-11-26 14:18:11	2210234.1
HD 35461	05194979−6626353	K1 III	5.683	2006-12-20 04:04:52	2210293.1
HD 35461 2				2006-12-18 23:57:17	2210298.1
HD 269376	05203372−6658537	A0 V	10.666	2006-12-08 12:28:56	2210269.1
HD 35665	05205607−6759034	K1.5 III	5.887	2006-11-24 15:59:18	2210228.1
HD 35905	05223623−6721285	K1 III	6.800	2006-12-01 05:07:47	2210252.1
HD 36207	05244398−6753507	K1 III	6.451	2006-11-23 05:15:04	2210226.1
HD 37122	05300077−6958319	K2 III	5.128	2007-04-25 09:40:22	2211408.1
HD 269704	05315890−6909392	K2 III	6.760	2006-11-03 18:51:36	2201172.1
HD 269704 2				2006-11-03 22:10:04	2201177.1
HD 269757	05335125−6946468	K1 III	8.187	2007-04-22 07:07:59	2211396.1
HD 37722	05344387−6928187	A4 V	8.640	2007-04-25 03:03:00	2211436.1
HD 37762	05344709−7010197	K0 III	5.565	2007-04-18 07:03:34	2211437.1
HD 269788	05345367−6846395	K4 III	6.331	2007-05-02 05:40:40	2211442.1
HD 269820	05355068−6929178	K1 III	7.185	2006-10-29 19:47:54	2201153.1
HD 269820 2				2006-10-30 18:56:54	2201154.1
HD 38861	05423256−7022555	K0 III	6.780	2007-04-08 06:53:36	2211365.1
HD 38993	05431866−7027254	K1.5 III	5.478	2007-04-06 05:12:23	2211360.1
HD 39980	05495921−6941060	K2 III	5.409	2006-10-09 18:39:20	2201097.1
HD 270186	05501123−6934296	K0 III	7.774	2006-10-09 18:39:20	2201097.1
for *L15*, *L24*					
HD 34461	05121801−6705415	K1 III	6.927	2006-06-03 06:16:38	2200068.1
HD 34461 2				2006-06-04 05:23:26	2200069.1
HD 34489	05122388−6756520	K2 III	6.169	2006-05-24 06:54:23	2200044.1
HD 34943	05153759−6804070	M0 III	3.970	2006-05-21 06:16:33	2200038.1
HD 35094	05164382−6811142	A3 V	8.554	2006-05-19 06:24:19	2200034.1
HD 35094 2				2006-05-19 08:03:24	2200035.1
HD 35323	05183268−6732320	M0 III	5.524	2006-12-04 17:29:51	2210261.1
HD 35323 2				2006-12-07 11:40:07	2210267.1
HD 269352	05193283−6752441	K5 III	6.014	2006-11-29 13:25:55	2210249.1
HD 35461	05194979−6626353	K1 III	5.683	2006-12-31 13:05:43	2210310.1
HD 35665	05205607−6759034	K1.5 III	5.887	2006-11-28 15:55:38	2210244.1
HD 35905	05223623−6721285	K1 III	6.800	2006-12-06 15:48:56	2210264.1
HD 36207	05244398−6753507	K1 III	6.451	2006-11-27 18:25:19	2210240.1
HD 37122	05300077−6958319	K2 III	5.128	2007-04-21 07:56:30	2211394.1
HD 37180	05302839−7011373	K0 III	6.851	2007-04-18 00:25:59	2211388.1
HD 269704	05315890−6909392	K2 III	6.760	2006-11-07 20:25:50	2201189.1
HD 37722	05344387−6928187	A4 V	8.640	2006-11-02 19:42:32	2201171.1
HD 37722 2				2006-11-03 05:37:54	2201176.1
HD 37762	05344709−7010197	K0 III	5.565	2007-04-12 06:57:26	2211376.1
HD 269788	05345367−6846395	K4 III	6.331	2006-11-08 22:53:20	2201186.1
HD 269820	05355068−6929178	K1 III	7.185	2006-11-02 19:42:32	2201171.1
HD 38861	05423256−7022555	K0 III	6.780	2007-04-02 06:48:19	2211351.1
HD 38993	05431866−7027254	K1.5 III	5.478	2007-04-02 05:08:54	2211350.1
HD 39980	05495921−6941060	K2 III	5.409	2006-10-16 22:35:50	2201114.1
HD 270186	05501123−6934296	K0 III	7.774	2006-10-18 19:14:15	2201115.1

7.5 pixels for MIR-S and MIR-L bands, respectively. We determined the sky value in an annulus just outside the aperture with a width of 5 pixels. The enclosed full widths at half maximum (FWHM) of the point spread function (PSF) were measured to be about 2.8–2.9 in the NIR bands, 2.0–2.3 in the MIR-S bands, and 2.2–2.9 in the MIR-L bands, respectively. These adopted radii include 98%, 95%–96% and 93%–94% of the stellar light in the NIR, MIR-S, and MIR-L bands, respectively, compared with the photometric results of the larger aperture radius of 15 pixels (T. Takagi 2008, unpublished internal report). It is necessary to emphasize here that our absolute calibration is based on the aperture photometry of point sources with a fixed aperture and sky annulus.

For the absolute calibration, a simple mean of the measured ADU values was used when the star was observed more than once. We also used both short and long exposure data when available. For a later discussion, we here define the instrumental magnitude as $-2.5\log(N_{\rm ADU}/t_{\rm exp})$. Throughout the paper, we use this magnitude if not specified.

4. Results and Discussion

4.1. Monitoring Observations: Stability Check

Figures 1–3 show the *light curves* of several bright stars in the monitoring fields in the *N2*, *S7*, and *L15* long bands, respectively. The ordinate is the magnitude difference of each star about its mean and the abscissa is the observed date counting from the launch date (UT). In the case of the *N2* band, we plot only stars with their standard deviations being less than 0.02 mag while 0.07 mag in the *S7* band and 0.1 mag in the *L15* band. The standard deviations of the brightest star in the *S7* and *L15* bands are 0.035 and 0.012, respectively. Thus, we did not detect a deviation of the instrumental magnitude from its mean value larger than 4% for at least bright stars. We stress here that the photometries were done independently and that no differential photometry was applied, as described in the previous section. We also made similar plots for long-exposure data of all the other bands and for short-exposure data of all NIR bands and found no deviation either. We also plot the short-term *light curves* of bright stars in the *N3* band in figure 4. This figure shows that the internal scatter in the observations of any one star is 1%. It should be mentioned that these short-term data were obtained with IRC00 and the signal-to-noise ratio is considered to be higher than that of the other data. These figures assure us to regard the sensitivity of all three channels of the IRC to be constant during Phases 1 and 2. Therefore, we ignore the time dependence of

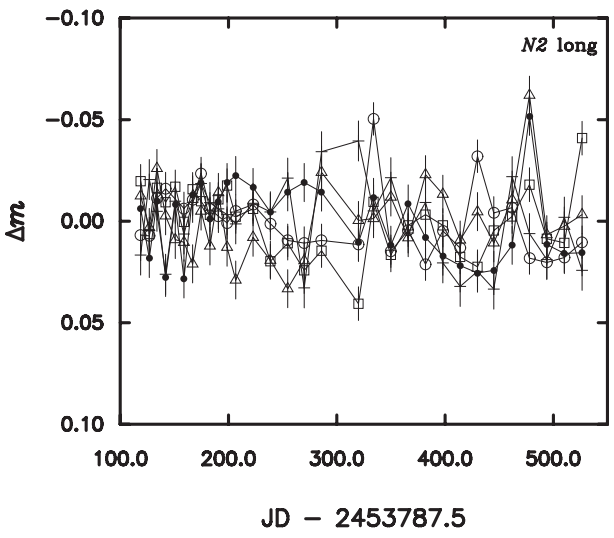

Fig. 1. Light curves of bright stars in the *N2* band/long exposure, which show the stability of the NIR channel. The ordinate is the magnitude difference of each star about the mean and the abscissa is the observed date counting from the launch. The standard deviation of n-times measurements of each star is plotted as an error bar. Filled circle: 17551760+6637195, open circle: 17551565+6639156, open square: 17553702+6640005, open triangle: 17555206+6636419, cross: 17552688+6636570.

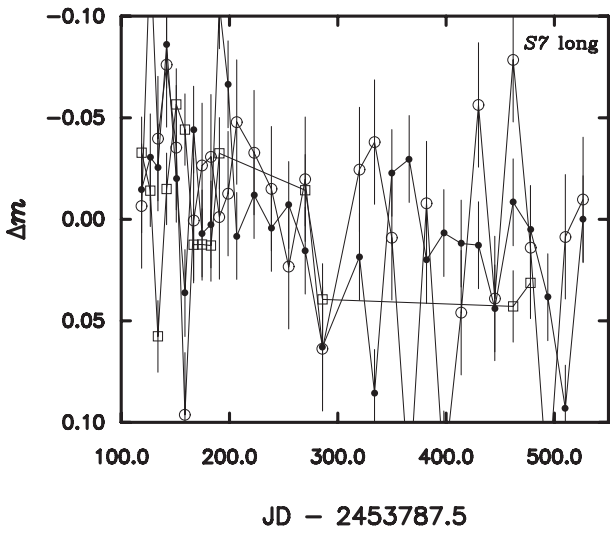

Fig. 2. Same as figure 1, but for the *S7* band/long exposure. Filled circle, 17554655+6638399; open circle, 17551760+6637195; open square, 17561794+6639037.

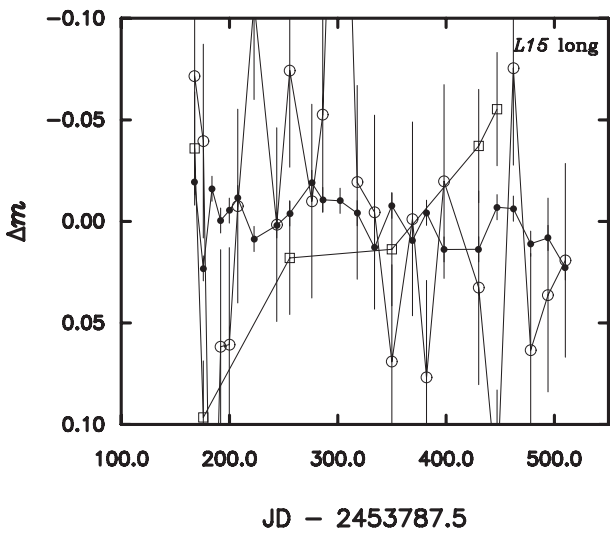

Fig. 3. Same as figure 1, but for the *L15* band/long exposure. Filled circle, 06005919−6636154; open circle: 06010083−6635434; open square, 06005625−6642158.

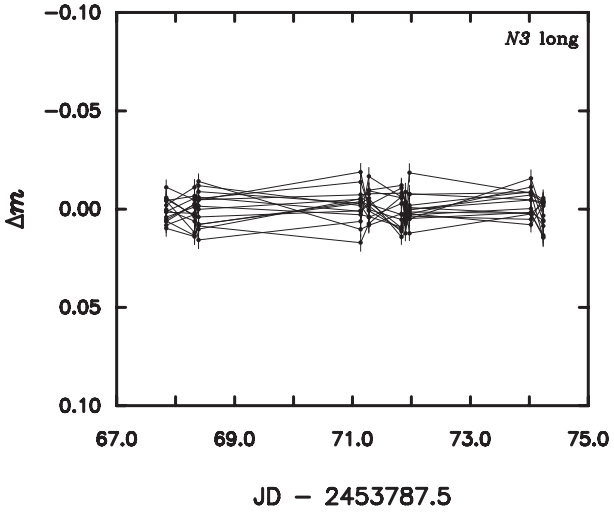

Fig. 4. Light curves of 15 bright stars in the *N3* band/long exposure within a week.

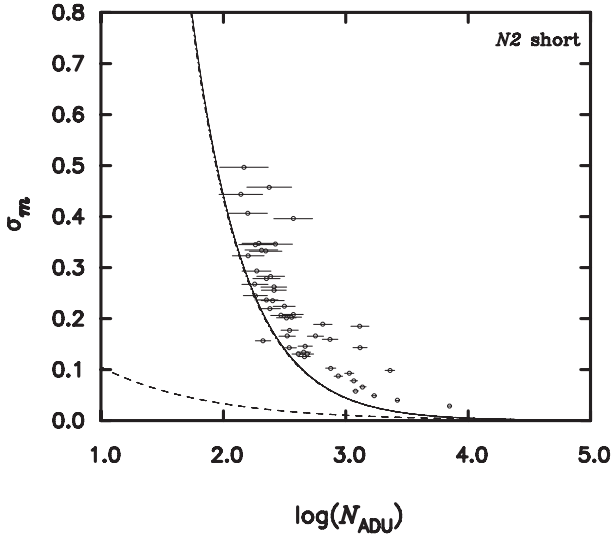

Fig. 5. Plot of the standard deviation of the magnitude measured in the light curves of stars in the monitoring field vs. logarithm of ADU values derived from the photometry for *N2* short exposure data. The solid curve is a theoretical estimate of the statistical error. The dashed and dash-dotted curves represent the case if stellar photon noise dominates, and if the read noise dominates, respectively, for a reference.

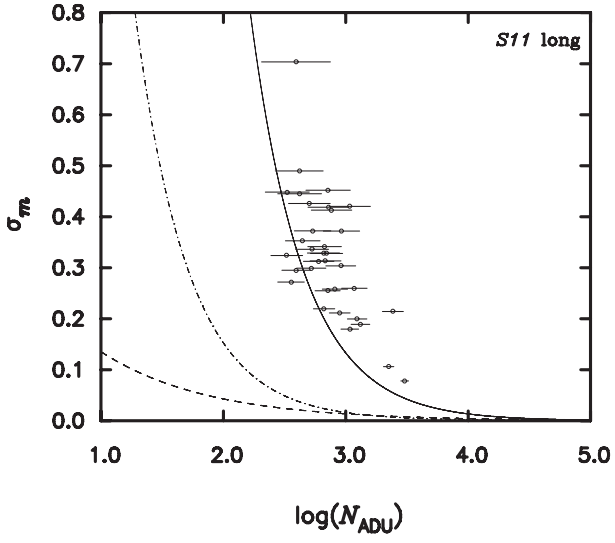

Fig. 6. Same as figure 5, but for the *S11* long exposure.

the sensitivity. We could not check short exposure data of the MIR-S and MIR-L bands because stars in the fields are too faint for a short exposure. However, we will show that the short and long-exposure data are consistent in subsection 4.3, which assures the same stability of short-exposure observations. We note that most stars in the NEP field are *normal* stars and thus they become faint in the MIR-S channel. This is the reason why the scatter in the *S7* band looks rather large compared to that in the *N2* band. When the observed $N_{\rm ADU}$ becomes small, the photometric error increases rapidly, which is discussed in subsection 4.2.

4.2. Intrinsic Uncertainty

Because the exposure time for all of the objects in a single frame is the same, each object will have a different signal-to-noise ratio, and thus a statistical error, derivable from its brightness. To check how this error depends on the observed ADU, we calculated the standard deviation of the magnitude of individual star using the data for monitoring observations. Figures 5 and 6 are such plots for the case of an *N2* short exposure where the read noise dominates and *S11* long exposure where the sky background dominates. In these figures, stars observed more than five times are plotted. These plots yield an empirical measurement of our photometric precision as a function of the observed ADU. It is evident that the standard deviation increases rapidly when the ADU value becomes small, say, below $\sim$1000.

Theoretically, the expected standard deviation, in magnitudes, of a given observation is given by the following equation (Howell 1993, 2006):

$$\sigma_m = 1.0857\,\frac{\sqrt{N_{\rm star}+p}}{N_{\rm star}}, \tag{1}$$

while

$$p = n_{\rm pix}\left(1+\frac{n_{\rm pix}}{n_{\rm sky}}\right)(N_{\rm sky}+N_{\rm D}+N_{\rm R}^2) \tag{2}$$

and $N_{\rm star}$ is the total number of electrons (photons) collected from the object of interest, $n_{\rm pix}$, the number of pixels in the aperture, $n_{\rm sky}$, the number of pixels used to estimate the sky level, $N_{\rm sky}$, the total number of electrons per pixel from the sky, $N_{\rm D}$, the total number of dark-current electrons per pixel, and $N_{\rm R}$, the total number of electrons per pixel resulting from the read noise. The number of electrons is the product of the ADU values and the gain, G. We list the values of the gain and the read noise of each channel/exposure configuration in table 4 (Wada et al. 2002). We simply divided equation (1) by $\sqrt{N_{\rm coadd}}$ to take account of the effect of co-addition. A solid curve in each figure is this estimation. For the case of an *N2* short exposure, we adopt $N_{\rm sky} \sim 3.0$ (ADU) and $N_{\rm coadd} = 3$, while for an *S11* long exposure, $N_{\rm sky} \sim 2300.0$ (ADU) and

Table 4. Gain and read noise of the IRC.

Channel	Exposure	Gain	$N_{\rm R}/e^-$
NIR	short	10.7194	30.6
	long		15.3
	long (IRC05)		7.65
MIR	short	6.43629	28.4
	long		14.2

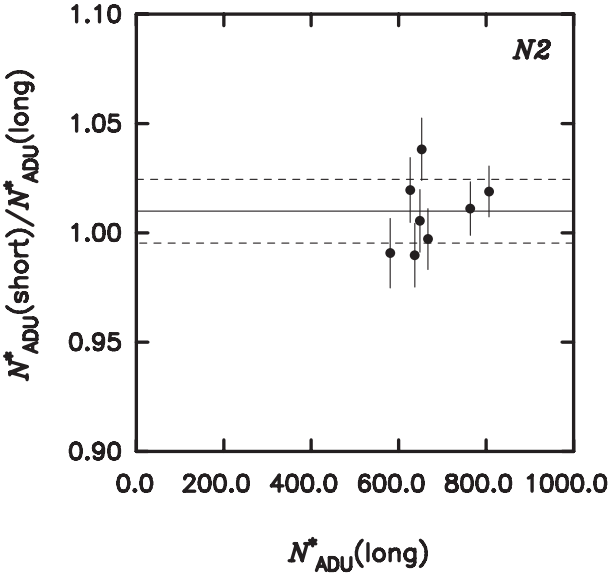

Fig. 7. Comparison of the photometric results between IRC03 short and long exposures in the *N2* band. A straight line shows a least-squares fitted value, and dashed lines are the 3-σ deviations.

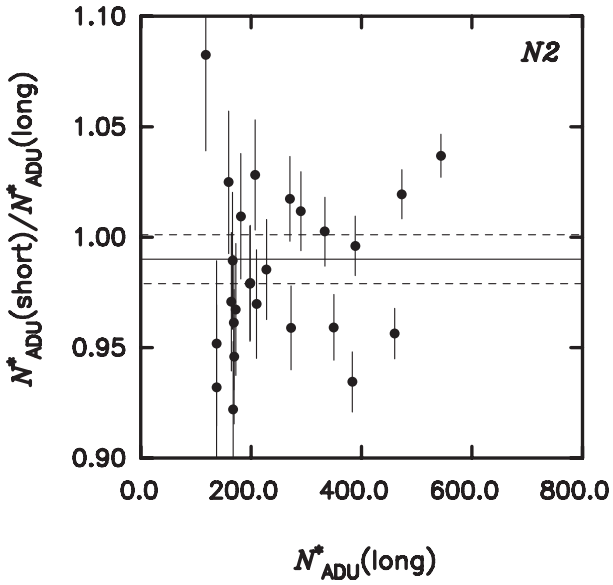

Fig. 8. Same as figure 7, but for IRC05 short- and long-exposure data.

Table 5. Reference wavelength and the range of integration.

Band	λ_i	$\lambda_{i_{\rm s}}$	$\lambda_{i_{\rm e}}$
N2	2.4	1.60	5.77
N3	3.2	1.60	5.77
N4	4.1	1.60	5.77
S7	7.0	2.50	23.86
S9W	9.0	2.50	23.51
S11	11.0	2.50	24.00
L15	15.0	2.50	23.76
L18W	18.0	2.50	28.72
L24	24.0	2.50	28.72

$N_{\rm coadd} = 6$, and we ignore $N_{\rm D}$. Although the observed values are somewhat large, a basic trend is well represented by this model in both cases. We note that we did not try to identify and remove any variable stars and that both figures are contaminated by those stars. We also plot the case if the read noise dominates over other terms ($N_{\rm sky} = 0$) by a dash-dotted curve, and if the stellar photon noise dominates ($p = 0$) by a dashed curve for a reference.

4.3. Consistency between Short and Long Exposure Times

To increase the number of standard star data for the absolute calibration, the simultaneous use of data obtained with short and long exposures is desirable when available. We have already mentioned in section 2, however, that the sampling methods of short and long exposures are slightly different and we have to check the consistency between them before merging the two data sets. To check it, we converted $N_{\rm ADU}$ derived independently from photometries of short and long-exposure data to $N^*_{\rm ADU}$ (normalized ADUs), and compared them. In figure 7, we plot the ratios of $N^*_{\rm ADU}$ of short exposure to long one of the identical stars vs. $N^*_{\rm ADU}$ (long) in the *N2* band. We used the data of standard stars in table 2, which were observed with IRC03. We applied a linear least-squares fit [assuming $N^*_{\rm ADU}$ (short) $= a\ N^*_{\rm ADU}$ (long)] to the data. The slope of the line is 1.010 ± 0.005 (1-σ), which is also shown in the figure. We checked for the consistency of all the other bands, and found that the deviations are less than 3%.

We did the same comparisons between the short and long-exposure data in the NIR channel obtained with IRC05, which is shown in figure 8 in the case of the *N2* band. For this purpose, LSNEP data were used. The slope of the fitted line is 0.989 ± 0.004, and the deviations of the other 2 bands are also less than 3%. The stars used in this analysis were from LSNEP fields and the range of brightness is much wider than that of standard stars. Therefore, this figure also assures that this consistency holds for such faint stars as $N_{\rm ADU} \sim 100$ in the short exposure.

Thus, we confirmed the consistency between the short and long exposure times of all the bands in the case of IRC03, and of all the NIR bands in the case of IRC05. This also verifies that the data were sampled as intended and the on-board controller of the IRC worked well. We did not check this consistency in the case of IRC02. However, the exposures were controlled by the same clock and we believe that this consistency also holds for observations with IRC02.

In the same way, we also checked the consistency of the long exposures between IRC03 and IRC05, and confirmed them.

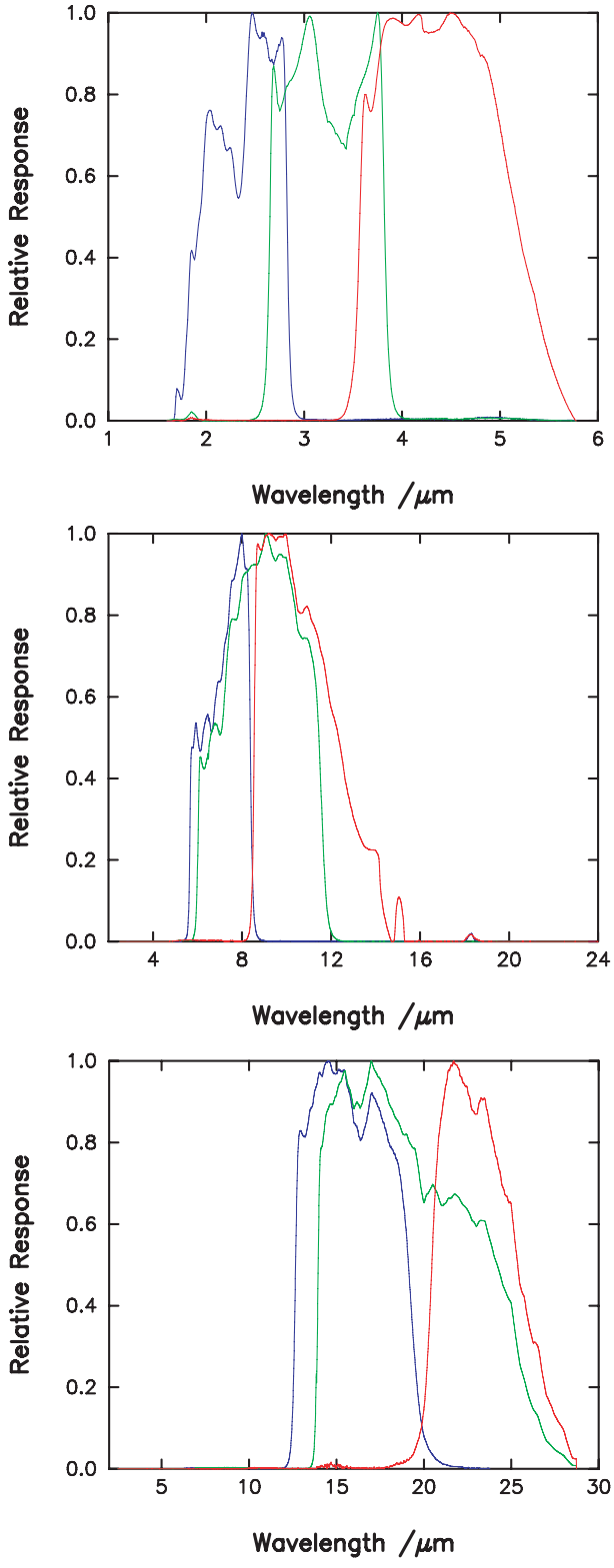

Fig. 9. Relative spectral response, R_i, of the IRC imaging bands. Top: NIR, middle: MIR-S, and bottom: MIR-L.

4.4. *Absolute Calibration*

For the absolute calibration, we compared the flux densities of standard stars with their observed ADU values to obtain

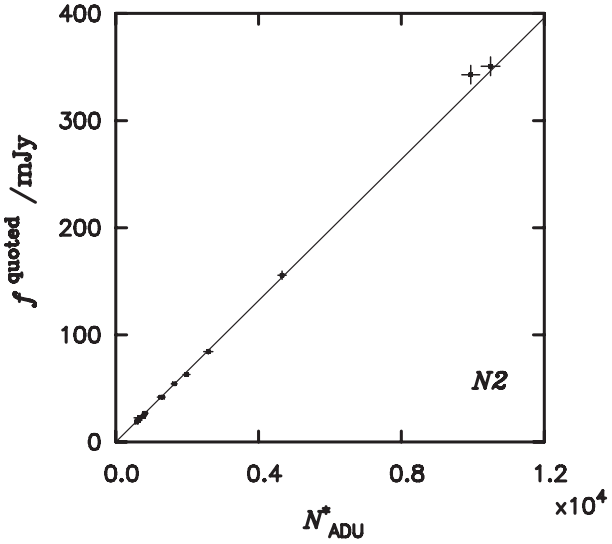

Fig. 10. Estimated flux density vs. observed ADU $t_{\rm IRC}^{-1}$ for the *N2* band. A solid line in each plot is a least-squares fit to the data after removing stars with a large deviation.

factors to convert the flux densities of all bands.

The flux density at the reference wavelength of each band, $f_{\lambda_i}^{\rm quoted}$, was calculated by the following equation:

$$f_{\lambda_i}^{\rm quoted} = \frac{\int_{\lambda_{i_s}}^{\lambda_{i_e}} \frac{R_i(\lambda)}{h\nu} f_\lambda(\lambda)\, d\lambda}{\int_{\lambda_{i_s}}^{\lambda_{i_e}} \left(\frac{\lambda_i}{\lambda}\right) \frac{R_i(\lambda)}{h\nu}\, d\lambda} \tag{3}$$

$$= \frac{\int_{\lambda_{i_s}}^{\lambda_{i_e}} R_i(\lambda)\, \lambda\, f_\lambda(\lambda)\, d\lambda}{\lambda_i \int_{\lambda_{i_s}}^{\lambda_{i_e}} R_i(\lambda)\, d\lambda}. \tag{4}$$

where $f_\lambda(\lambda)$ is the flux density of a standard star (Cohen template) and $R_i(\lambda)$ is the spectral response of band i. Each $R_i(\lambda)$ takes into account the transmission of the optics and the response of the detector, and is given in units of electrons per photon.[4] Here, $f_\nu \propto \nu^{-1}$ or $f_\lambda \propto \lambda^{-1}$ is assumed. This is the convention adopted by IRAS and is used by several infrared astronomical satellites such as COBE, ISO, and Spitzer/IRAC since then. Because of this, we refer it as the *quoted* flux density. The reference wavelength of each band, λ_i, is listed in table 5 along with the range of the integration (λ_{i_s}, λ_{i_e}). The wavelength ranges of the integrations are chosen to be wide enough to include recognized blue and red leaks of the filters (Onaka et al. 2007). Plots of the relative spectral response of all the bands are given in figure 9.

To use both short and long-exposure data, if available, we converted $N_{\rm ADU}$ to $N_{\rm ADU}^*$ (normalized ADUs), and compared them to the estimated flux densities. Figure 10 is such an example in the case of the *N2* band. We assumed that the error of the estimated flux density of the standard star is 5%

[4] ⟨http://www.ir.isas.jaxa.jp/ASTRO-F/Observation/RSRF/IRC_FAD/⟩, unit: electron per energy, i.e., $R_i(\lambda)/h\nu$.

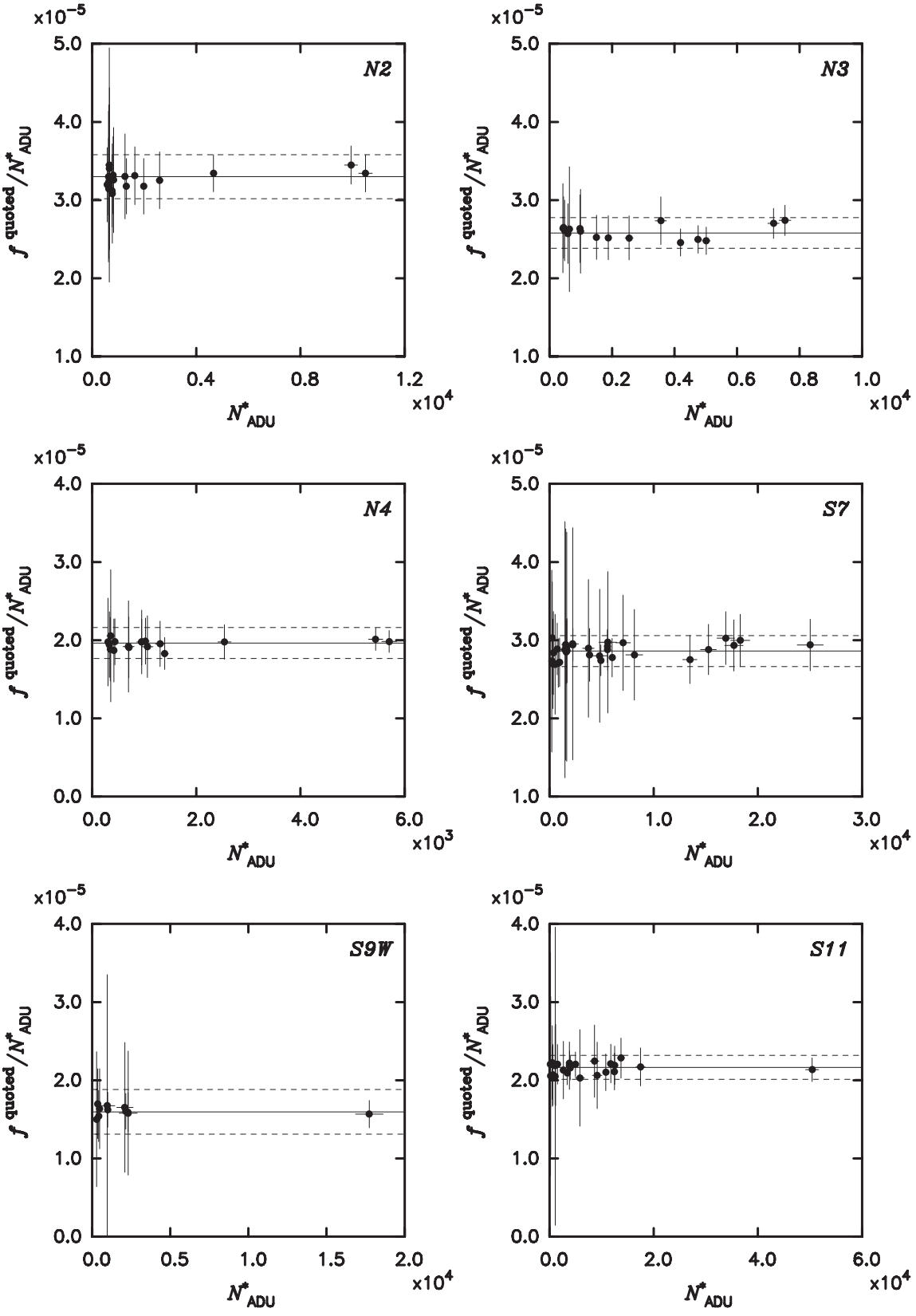

Fig. 11. Comparison of the estimated flux density with the observed ADU $t_{\rm IRC}^{-1}$ for the *N2*, *N3*, *N4*, *S7*, *S9W*, *S11*, *L15*, *L18W*, *L24* bands. A solid line in each plot is a least-squares fitted value, and the dashed lines are the 3-σ deviations.

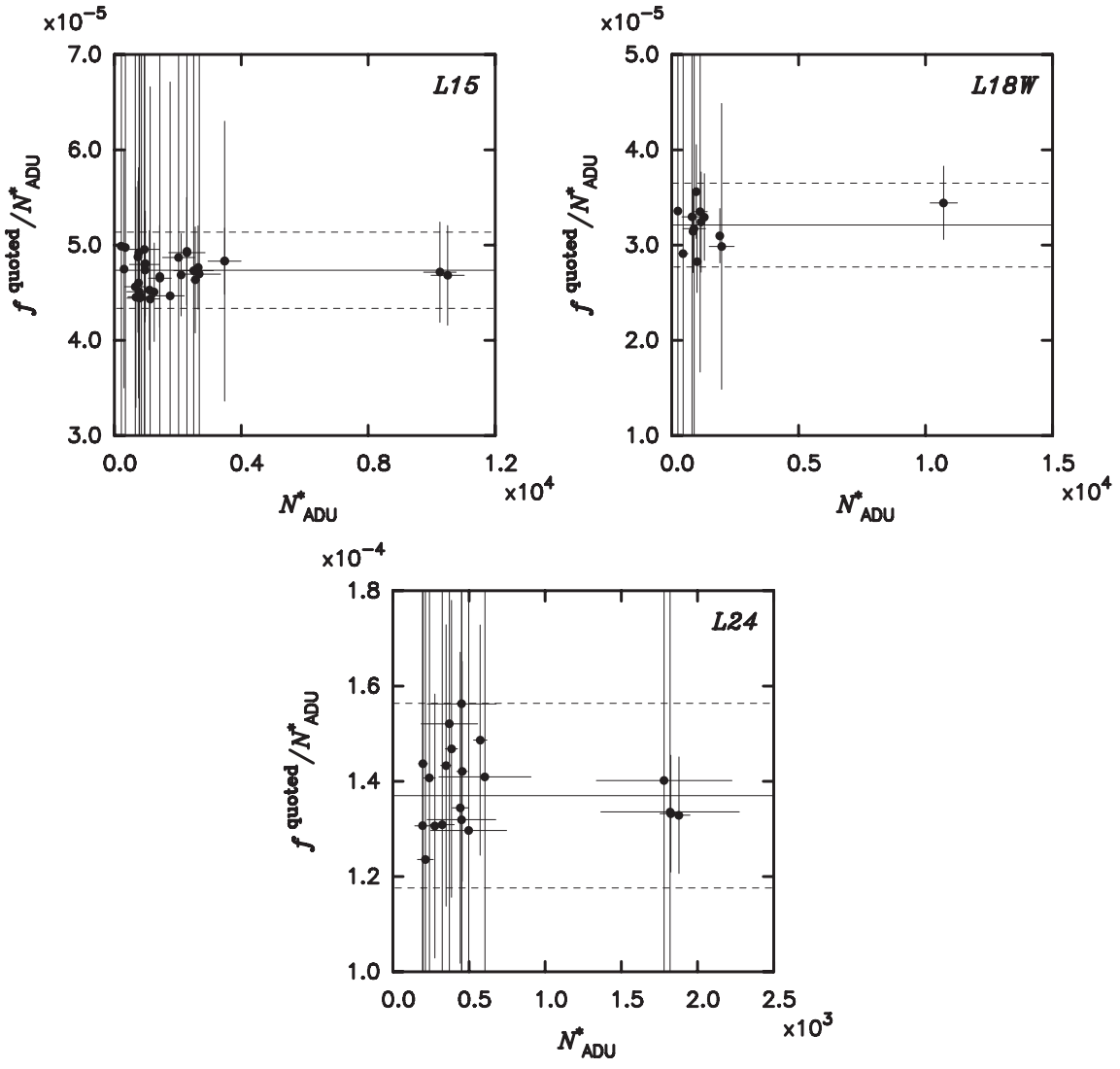

Fig. 11. (Continued)

taking into account the uncertainties of both the template of the standard stars and the spectral response, $R_i(\lambda)$. Observational errors are adopted from their ADU values (see subsection 4.2). A straight line ($f_{\lambda_i}^{\rm quoted} = a\ N_{\rm ADU}^*$) was fitted to these data, which is also shown in the figure. In this fitting, we first applied a least-squares fit, and then stars with deviations larger than 3-times the fitting error were omitted, and we applied a fitting again. We list the adopted and rejected stars in the appendix. In figure 11, we plot the ratios of $f_{\lambda_i}^{\rm quoted}$ to $N_{\rm ADU}^*$ vs. $N_{\rm ADU}^*$ of standard stars for each band along with the fitted slope value and the deviations. The slope value provides the conversion factors (CFs), f_0 (ADU $t_{\rm IRC}^{-1}$ to Jy), which are tabulated in table 6 along with the fitting errors. The number of standard stars in the *S9W* and *L18W* bands is small compared with the others because no SAGE standard is available, and the error of the *S9W* band is somewhat larger. However, we believe that the accuracies of the CFs are good enough to obtain the flux densities in most cases. Also, the uncertainties of these factors are rather small compared with, for example, the intrinsic errors

Table 6. Conversion factor, f_0 (ADU $t_{\rm IRC}^{-1}$ to Jy).

Band	f_0	Error (%)	$N_{\rm star}$*
N2	3.300×10^{-5}	2.84	19
N3	2.580×10^{-5}	2.54	16
N4	1.964×10^{-5}	3.35	17
S7	2.861×10^{-5}	2.30	31
S9W	1.596×10^{-5}	5.97	11
S11	2.165×10^{-5}	2.36	25
L15	4.735×10^{-5}	2.82	33
L18W	3.210×10^{-5}	4.56	13
L24	1.370×10^{-4}	4.72	20

* Number of standard stars used.

Table 7. Conversion factors ($N_{\rm ADU}$ to Jy) calculated from f_0.

Band	Short exposure $f_{\rm s}$	Long exposure $f_{\rm l}$	Long exposure IRC05 $f'_{\rm l}$	Error (%)
N2	4.125×10^{-6}	4.342×10^{-7}	2.946×10^{-7}	2.84
N3	3.225×10^{-6}	3.394×10^{-7}	2.303×10^{-7}	2.54
N4	2.455×10^{-6}	2.584×10^{-7}	1.753×10^{-7}	3.35
S7	2.861×10^{-5}	1.022×10^{-6}		2.30
S9W	1.596×10^{-5}	5.700×10^{-7}		5.97
S11	2.165×10^{-5}	7.732×10^{-7}		2.36
L15	4.735×10^{-5}	1.691×10^{-6}		2.82
L18W	3.210×10^{-5}	1.146×10^{-6}		4.56
L24	1.370×10^{-4}	4.892×10^{-6}		4.72

Table 8. Quoted flux densities, actual flux densities, and color correction factor.*

Band	λ_i	$f_{\lambda_i}^{\rm quoted}$/Jy	f_{λ_i}/Jy	K_{λ_i}
N2	2.4	611.09	554.11	1.103
N3	3.2	343.34	334.12	1.028
N4	4.1	184.73	212.23	0.870
S7	7.0	74.956	77.000	0.974
S9W	9.0	56.262	47.337	1.189
S11	11.0	38.258	32.006	1.195
L15	15.0	16.034	17.314	0.926
L18W	18.0	12.001	12.115	0.991
L24	24.0	8.0459	6.8303	1.178

* Of the model Vega template at the reference wavelength, λ_i. Color corrections are given for each band.

and/or the color correction. Using these CFs and taking into account the unit number, we calculated the conversion factors, $f_{\rm s}$ (ADU to Jy for short-exposure data) and $f_{\rm l}$ (ADU to Jy for long exposure data) which are tabulated in table 7. We note that we did not use the value of $t_{\rm IRC}$ for this absolute calibration.

The flux density obtained using these derived conversion factors is a *quoted* flux density at the reference wavelength and equal to the actual flux density only when the source has a $\nu f_\nu = $ const. spectrum. Furthermore, the reference wavelength of each band adopted for the AKARI IRC is just a representative one and does not have any physical meaning. For these two reasons, a color correction is needed if we want to know the real flux density at the reference wavelength. The color correction factor for Vega (A0 V) at each band is also tabulated in table 8 and we can see that it amounts to 20% in some cases. Note that normal stars, if not particularly red, have more or less a similar spectral energy distribution to Vega in the infrared.

We want to stress that our photometry is performed to a point source with a fixed aperture and sky annulus. Therefore, these conversion factors should be applicable only to a measurement done with the same parameters. Photometry using the different aperture and sky annulus will need an aperture correction. These conversion factors can not be used for extended sources, either.

4.5. AKARI Magnitude System

As mentioned above, the flux density calculated using the derived conversion factor is a *quoted* flux density, $f_{\lambda_i}^{\rm obs}$. In this system, the magnitude at each reference wavelength is calculated by

$$[\lambda_i] = -2.5 \log_{10} \left(\frac{f_{\lambda_i}^{\rm obs}}{f_{\lambda_i}^{\rm quoted}} \right), \quad (5)$$

where $f_{\lambda_i}^{\rm quoted}$ is the *quoted* flux density of Vega, the so-called zero-magnitude flux for the AKARI IRC system. Using the Kurucz synthetic spectrum of Vega (Cohen et al. 1992) and equation (4), we calculated $f_{\lambda_i}^{\rm quoted}$ at each reference wavelength and list them in table 8. The magnitude is defined as the ratio of the "in-band" flux of a source to that of Vega and we don't have to consider its spectrum. Because the magnitude in this system is based on the Vega spectrum, it can be used along with the standard system in the visible and near-infrared wavelengths. For a reference, the actual flux density at each reference wavelength, f_{λ_i}, taken from the model Vega template, is also listed in the table.

Ita et al. (2008) cross-identified AKARI LSLMC survey data with the Spitzer SAGE survey catalog (Meixner et al. 2006), and compared the magnitudes of closely matched bands, *N3* and *[3.6]*, and *S7* and *[8.0]*, respectively in their figure 7. They found that both magnitudes are very close for most stars and that the differences concentrated around zero in both bands although the bandpasses of both cameras are different. This may give indirect evidence that the absolute calibration done here is consistent with that of Spitzer/IRAC (Reach et al. 2005).

5. Summary

We performed an absolute calibration of the Infrared Camera (IRC) aboard the AKARI satellite. We observed one NEP field and one SEP field regularly for checking the stability of the IRC, and observed a set of standard stars for the absolute calibration. All of the data were reduced, and photometries were performed in the same manner.

For a stability check, we monitored the brightnesses of identical stars within the NEP and SEP fields and found that at

Table 9. Adopted stars in the NIR and MIR-S bands.*

Star	*N2*		*N3*		*N4*		*S7*		*S9W*		*S11*	
	Short	Long	Short	Long	Short	Long	Short	Long	Short	Long	Short	Long
HD 42525	S	S	S	S	S	S	◯	S	◯	S	◯	S
NPM1 +60.0581	◯	S	◯	S	◯	◯	w	◯	w	◯	w	+4.17
1757132	◯	◯	w	◯	w	◯	w	w	w	w	w	w
KF 03T1	◯	S	◯	S	◯	◯	w	◯	w	◯	w	◯
KF 03T2	◯	S	◯	S	◯	S	w	◯	◯	◯	w	◯
KF 06T1	◯	◯	◯	+3.08	w	◯	w	w	w	w	w	w
KF 06T2	◯	◯	w	◯	w	◯	w	w	w	w	w	w
KF 06T3	◯	◯	◯	◯	◯	◯	w	◯	w	◯	w	w
KF 03T3	◯	◯	w	◯	w	◯	w	w	w	w	w	w
KF 03T4	◯	S	+3.45	S	◯	◯	w	◯	w	◯	w	◯
KF 09T1	◯	S	◯	S	◯	S	◯	◯	◯	◯	w	◯
KF 06T4	w	◯	w	◯	w	◯	w	w	w	w	w	w
KF 01T4	◯	S	+3.02	S	◯	S	◯	◯	◯	◯	w	◯
KF 01T5	◯	◯	w	+3.73	w	◯	w	w	w	w	w	w
HD 34461			S	S			◯	◯			w	◯
HD 34555			◯	S			w	◯			w	−4.58
HD 34943			S	S			S	S			◯	S
HD 269247			−3.07	S			w	−6.12			w	−6.69
HD 35094			◯	S			c	c			w	c
HD 35183			◯	S			w	◯			w	◯
HD 35323			S	S			◯	S			◯	S
HD 269352			S	S			x	S			−4.84	S
HD 35461			S	S			◯	S			◯	S
HD 269376			−4.13	−3.89			w	w			w	w
HD 35665			S	S			+3.76	S			◯	S
HD 35905			S	S			+3.81	◯			w	◯
HD 36207			S	S			◯	S			w	◯
HD 37122			S	S			◯	S			◯	S
HD 269704			S	S			◯	◯			w	◯
HD 269757			◯	S			+3.98	◯			w	◯
HD 37722			◯	S			w	◯			w	◯
HD 37762			S	S			◯	S			◯	S
HD 269788			S	S			◯	S			◯	S
HD 269820			S	S			◯	◯			w	◯
HD 38861			S	S			+3.13	◯			w	◯
HD 38993			S	S			◯	S			◯	S
HD 39980			S	S			+3.59	S			◯	S
HD 270186			S	S			◯	◯			w	◯

* ◯: Adopted for the fitting.
+ followed by the the number of standard deviations: predicted calibrator flux is this many standard deviations larger than the fitted line.
− followed by the the number of standard deviations: predicted calibrator flux is this many standard deviations smaller than the fitted line.
w: Too faint.
S: Saturated.
c: Contaminated by the extended emission.
x: No data because of co-add failure.

least several bright stars do not show any brightness change within 4%. Thus, we concluded that the sensitivities of all the bands were constant and that the IRC were very stable during Phases 1 and 2.

Using the data of these repeated observations, we presented an example for evaluating the intrinsic errors due to the observed ADU values. We found that the errors increase rapidly toward fainter objects and this trend is well described by the current theoretical model.

We also checked the consistency between short and long exposure times and confirmed this for observations operated with IRC03 and IRC05. This also verifies that the on-board controller of the IRC worked well.

For the absolute calibration, we compared the estimated in-band flux densities with the observed ADU values of the standard stars at all bands. From these comparisons, we derived

Table 10. Adopted stars in the MIR-L bands.*

Star	*L15*		*L18W*		*L24*	
	Short	Long	Short	Long	Short	Long
HD 42525	◯	−3.14	◯	◯	w	−3.60
NPM1 +65.0451	◯	◯	−5.49	◯	w	w
HD 158485	−3.88	◯	−3.74	◯	w	◯
BD +66 1060	◯	−3.13	◯	◯	w	w
NPM1 +67.0536	◯	◯	◯	◯	w	◯
HD 165459	−6.10	−4.52	◯	◯	w	−7.57
BD +66 1073	w	◯	w	◯	w	w
KF 01T4	w	◯	w	◯	w	w
HD 166780	◯	S	◯	S	◯	◯
HD 34461	◯	◯			w	w
HD 34489	◯	◯			−5.49	◯
HD 34943	◯	S			◯	◯
HD 35094	w	c			w	w
HD 35323	◯	◯			◯	◯
HD 269352	−3.05	−3.56			−4.93	◯
HD 35461	◯	◯			w	◯
HD 35665	+6.23	+5.55			w	◯
HD 35905	+3.11	◯			w	w
HD 36207	◯	◯			w	w
HD 37122	◯	◯			◯	◯
HD 37180	+7.03	+3.65			w	w
HD 269704	◯	◯			w	w
HD 37722	w	w			w	w
HD 37762	◯	◯			◯	◯
HD 269788	−4.28	−3.68			w	◯
HD 269820	−3.49	−5.75			w	w
HD 38861	◯	◯			w	w
HD 38993	◯	◯			◯	◯
HD 39980	+5.16	+3.25			◯	+4.06
HD 270186	w	◯			w	w

*The symbols are the same as those in table 9.

conversion factors from the observed ADUs to the flux densities of all the band/exposure configurations. The absolute uncertainties of these factors are less than 6%, fairly small compared with, for example, the intrinsic errors and color correction.

AKARI is a JAXA project with the participation of ESA. We thank all members of the AKARI project for their continuous help and support. M. Cohen thanks both JAXA and the University of Tokyo for hosting several visits to Japan so that he could participate actively in the calibration of the IRC. T. Takagi is supported by a Japan Society for the Promotion of Science (JSPS) Fellowships for Research. This work is supported in part by a Grant-in-Aid for Scientific Research on Priority Areas from the Ministry of Education, Culture, Sports, Science and Technology and Grants-in-Aid for Scientific Research from the JSPS.

Appendix. Adopted and Rejected Standard Stars

We list the standard stars used for the absolute calibration in the NIR, MIR-S bands, and the MIR-L bands in tables 9 and 10, respectively. Stars with marks, except for w (too faint) and S (saturated), were tried for the first fitting to derive conversion factors, but stars with − and + were found to deviate from the fitted line and were not adopted. The figures following these letters are the values of the deviation from the fitted line defined as

$$\left(\frac{f_{\lambda_i}^{\mathrm{quoted}}}{N_{\mathrm{ADU}}^{*}} - a\right) \Big/ \sigma, \tag{A1}$$

where a is the slope of the fitted line and σ is the fitting error.

References

Cohen, M. 2003, in Proc. The Calibration Legacy to the ISO Mission, ed. L. Metcalfe, A. Salama, S. B. Peschke, & M. F. Kessler, ESA SP-481 (Noordwijk: ESA Publ.), 135
Cohen, M., Megeath, S. T., Hammersley, P. L., Martín-Luis, F., & Stauffer, J. 2003a, AJ, 125, 2645
Cohen, M., Walker, R. G., Barlow, M. J., & Deacon, J. R. 1992, AJ, 104, 1650
Cohen, M., Walker, R. G., Carter, B., Hammersley, P., Kidger, M., & Noguchi, K. 1999, AJ, 117, 1864
Cohen, M., Wheaton, Wm. A., & Megeath, S. T. 2003b, AJ, 126, 1090
Cohen, M., Witteborn, F. C., Carbon, D. F., Davies, J. K., Wooden, D. H., & Bregman, J. D. 1996, AJ, 112, 2274
Fowler, A. M., & Gatley, I. 1990, ApJ, 353, L33
Howell, S. B. 1993, in IAU Colloq. 136, Stellar Photometry — Current Techniques and Future Developments, ed. C. J. Butler & I. Elliott (Cambridge: Cambridge University Press), 318
Howell, S. B. 2006, in Handbook of CCD Astronomy, Second Edition (Cambridge: Cambridge University Press), ch. 4.4
Ita, Y., et al. 2008, PASJ, 60, (#3377)
Klemola, A. R., Jones, B. F., & Hanson, R. B. 1987, AJ, 94, 501
Kümmel, M. W., & Wagner, S. J. 2000, A&A, 353, 867
Matsuhara, H., et al. 2007, PASJ, 59, S543
Meixner, M., et al. 2006, AJ, 132, 2268
Murakami, H., et al. 2007, PASJ, 59, S369
Ohyama, Y., et al. 2007, PASJ, 59, S411
Onaka, T., et al. 2007, PASJ, 59, S401
Reach, W. T., et al. 2005, PASP, 117, 978
Wada, T., et al. 2002, Adv. Space Res., 30, 2111